—Supporting Information—

Role of point defects in spinel Mg chalcogenide conductors

Pieremanuele Canepa,[*,†,‡,‖] Gopalakrishnan Sai Gautam,[¶,†,‡] Danny Broberg,[§] Shou-Hang Bo,[†] and Gerbrand Ceder[*,†,¶,§]

† *Materials Science Division, Lawrence Berkeley National Laboratory, Berkeley, CA 94720, USA*

‡*Contributed equally to this work*

¶ *Department of Materials Science and Engineering, Massachusetts Institute of Technology, Cambridge, MA 02139, USA*

§*Department of Materials Science and Engineering, University of California Berkeley, Berkeley, CA 94720, USA*

‖*Current address: Department of Chemistry, University of Bath, Bath, BA2 7AY, UK.*

E-mail: pcanepa@lbl.gov; gceder@berkeley.edu

S1 Example of Freysoldt Correction

Figure S1 represents the DFT, long-range and short-range electrostatic potential components for the Vac''_{Sc} (q = –2) in $MgSc_2Se_4$, as referenced to the bulk neutral structure. The short-range component, i.e., the difference between the DFT and the long-range components, converges to a value $C \sim -0.09$ V, far away from the defect and its periodic image (0 and 16 Å on the x-axis). The magnitude of C, as indicated by the dashed black line, leads to a $E_{corr} = \mathrm{q} \times C \sim 0.18$ eV for the Vac''_{Sc} defect.[1] Similar E_{corr} values are evaluated for all charged defects considered in this work.

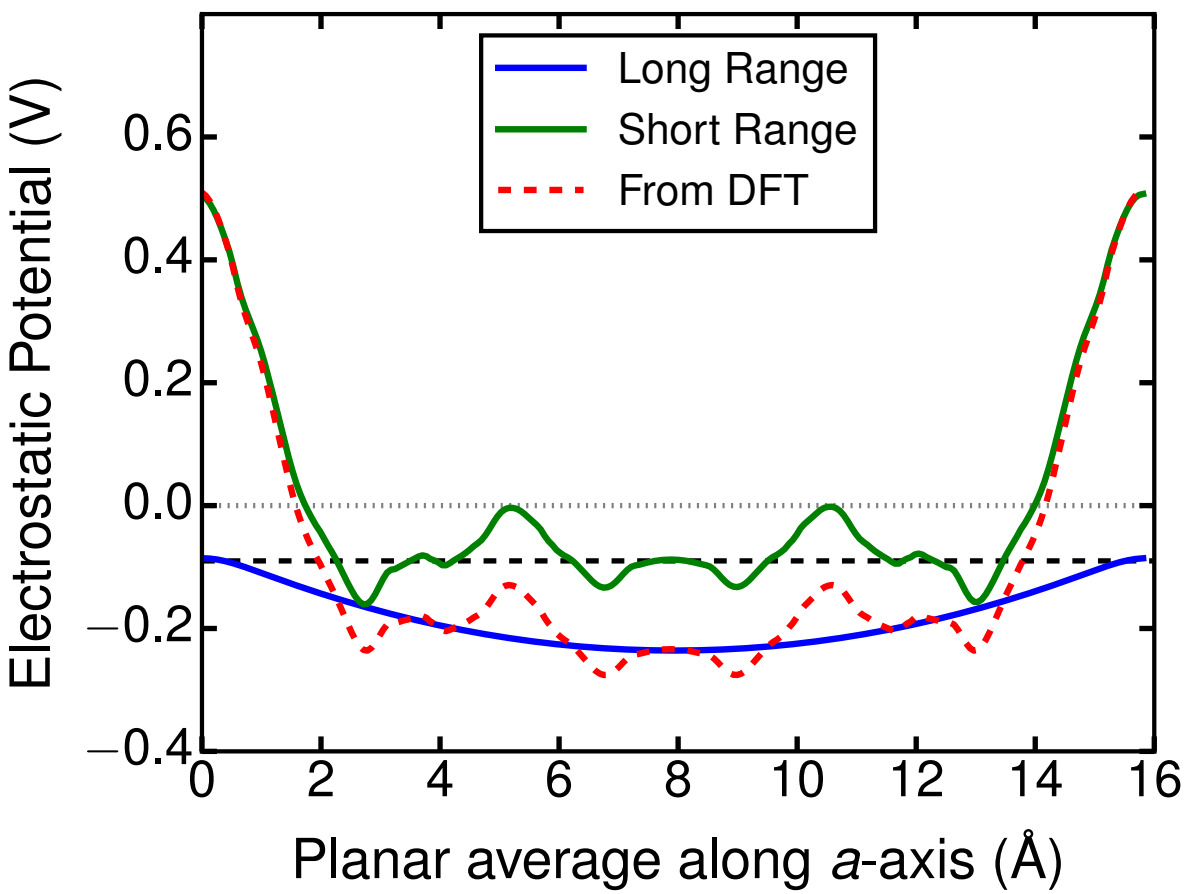

Figure S1: Evolution of the electrostatic potential for Vac_{Sc} (q = –2) in $MgSc_2Se_4$. The electrostatic potential is represented through averages over a transversal plane, i.e., along the a-axis of a cubic spinel cell. The defect is located at the origin and its first periodic image is found at $\sim$ 16 Å, corresponding to a calculation done in a $2 \times 2 \times 2$ supercell.

S2 Sample defect energies

Figure S2 illustrates the defect energy diagram,[2] with the defect formation energies (y-axis) plotted as a function of the Fermi energy of the bulk structure (x-axis). The Fermi energy is set arbitrarily to 0 eV at the Valence Band Maximum, VBM. E_{gap} on the x-axis indicates the magnitude of the band gap (white region) of the insulator and the energy of the Conduction Band Minimum, CBM. The grey regions on both sides of the band gap are the Valence Band (VB, Fermi energy < 0) and the Conduction Band (CB, Fermi energy $> E_{gap}$) of the material. Point defects can occur as neutral as well as charged species. For example, the solid

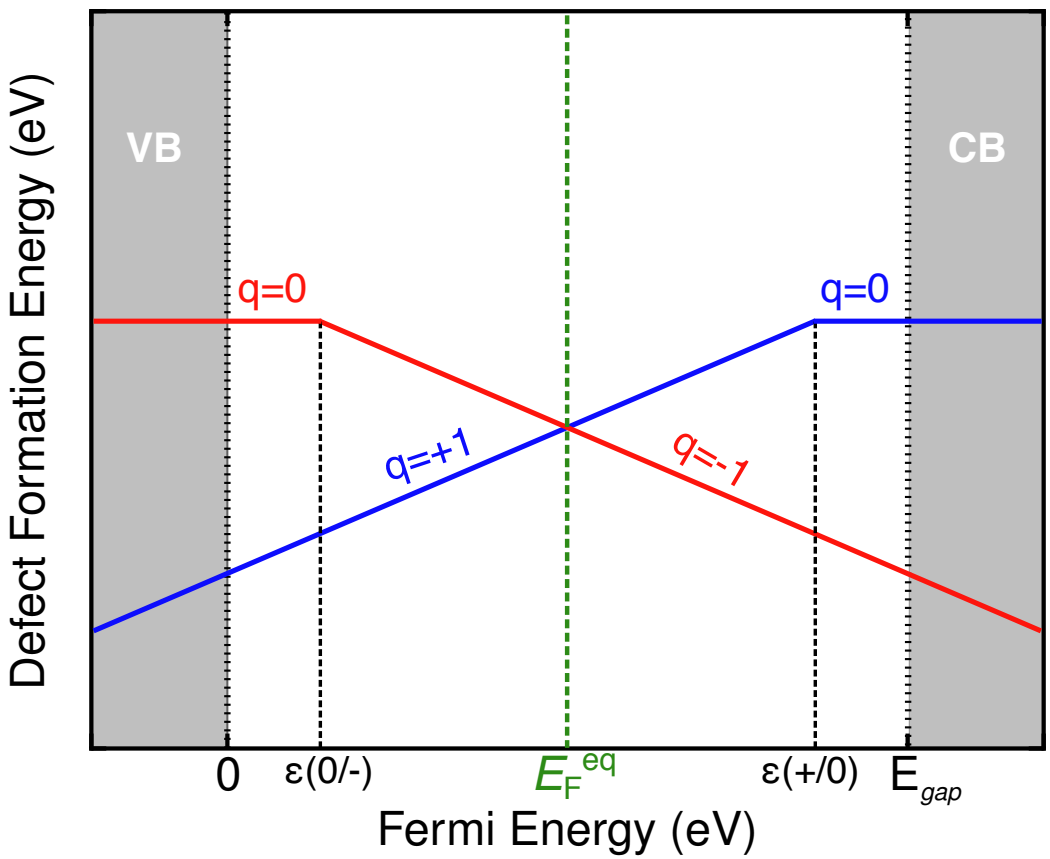

Figure S2: Scenario of self-compensating donor (blue) and acceptor (red) defects in a semiconductor with a band gap, E_{gap}. The defect formation energy (Equation 1 in manuscript) on the y-axis is plotted as a function of the Fermi energy on the x-axis, where the top of the valence band is arbitrarily set to 0 eV and the minimum of the conduction band is at E_{gap}.

blue line in Figure S2 represents a donor defect (such as $P^{\bullet}_{Si}$ or equivalently $Sc^{\bullet}_{Mg}$). Across the gap, for Fermi energy $< \epsilon(+/0)$, the donor defect is positively charged (i.e., $q = +1$ or

$P^{\bullet}_{Si}$), while for Fermi energy $> \epsilon(+/0)$, the defect is neutral ($q = 0$, $P^{\times}_{Si}$). Conventionally, a donor atom has a higher number of valence electrons than the atom being substituted (e.g., P has 5 valence electrons to Si's 4 and Sc has 3 compared to Mg's 2). As a result, a positively charged defect will correspond to the donor atom exchanging the excess electron with the electron reservoir of the structure, whose energy is set by the equilibrium Fermi energy. In contrast, a neutral defect implies that the excess valence electron localizes on the donor site. Analogous comparisons can be made for acceptor defects (such as B'_{Si} and Mg'_{Sc}), where the negatively charged defect corresponds to the acceptor atom exchanging a deficit electron (or excess hole) with the electron reservoir.

The thermodynamic defect transition level is the the Fermi energy at which different charge states of a defect have equal formation energy (indicated as $\epsilon(+/0)$ for donor defects and ($\epsilon(0/-)$) for acceptor). A defect transition level, in the absence of other energetically comparable defects in the structure, sets the equilibrium Fermi level within the gap, thus influencing the electronic conductivity of the parent structure. Thermal ionization of free charge carriers can naturally occur if the defect transition level sits within $\approx k_{\mathrm{B}}\mathrm{T}$ from the CBM (free electrons, e^-) or VBM (free holes, h^+), respectively.

In the presence of multiple defects (with low defect formation energies across the gap) the equilibrium Fermi level must be calculated self-consistently, in turn setting the defect concentrations, free carrier concentrations, and electronic conductivity of the material. An example of two defects with opposite charges, i.e., one each of n- and p-type, across the band gap is shown in Figure S2. Under equilibrium, the n-type defect (solid blue line in Figure S2) can "compensate" the equivalent opposite charge of the p-type defect (solid red line), commonly referred to as "charge-compensation", in order to maintain the charge neutrality of the overall crystal. The compensating behavior of charged defects leads to "pinning" the equilibrium Fermi level within the gap, as indicated by $E_{\mathrm{F}}^{\mathrm{eq}}$ in Figure S2 (dashed green line), eventually determining the electronic properties of the material.

S3 Band Structure and Density of States

Figure S3 Band Structure and Density of States of MgA_2Z_4 (A = Sc/In, Z = S/Se) obtained with the semi-local PBE[3] (left panels) and the hybrid HSE06[4,5] (right panels) functionals.

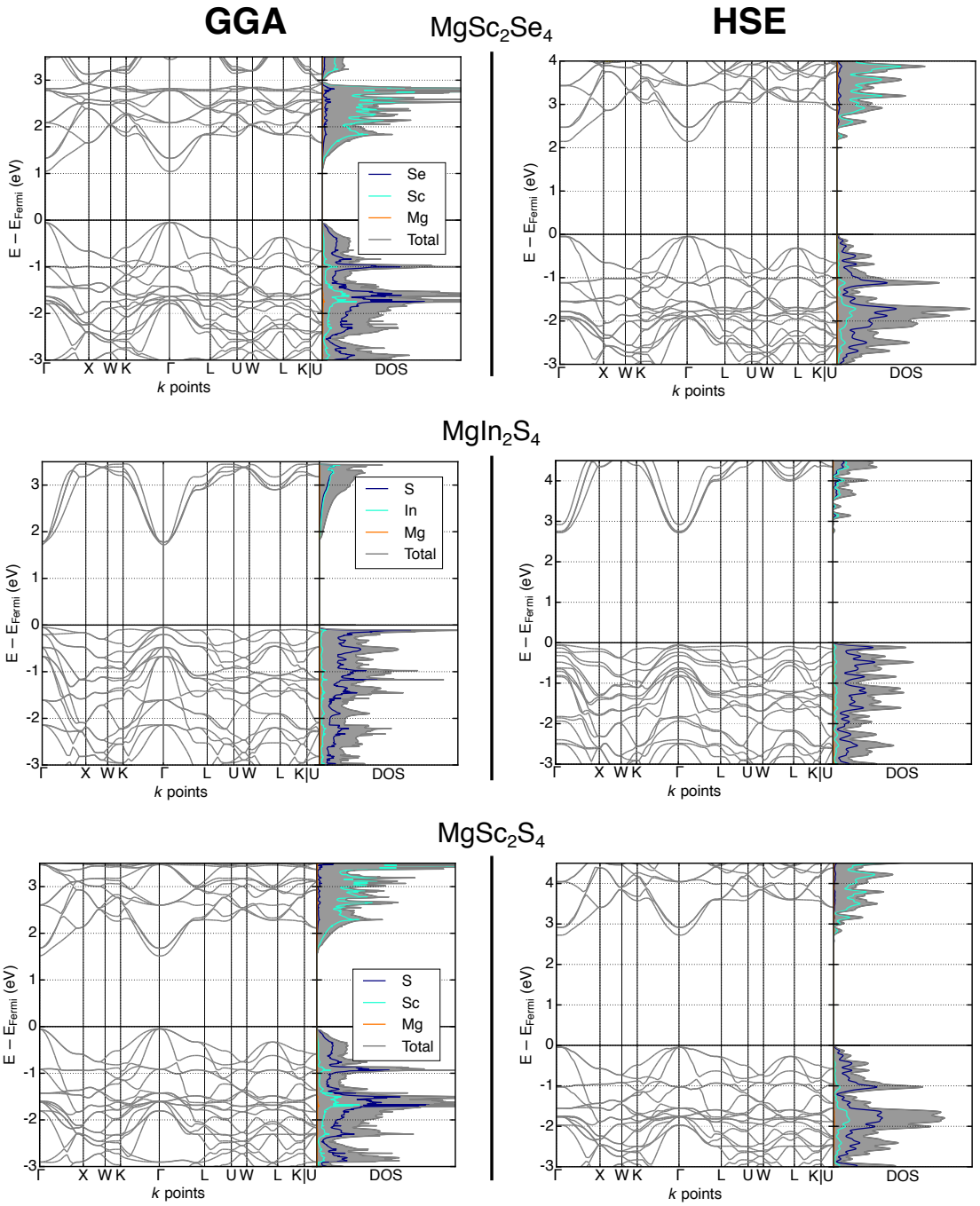

Figure S3: Left panels semi-local GGA PBE and Right panels Hybrid HSE06 Band Structures (along the k-path Γ-X-W-K-Γ-L-U-W-L-K-U) and Projected Density of States for MgA_2Z_4 compounds, with A = Sc or In and Z = Se or S. VBM set arbitrarily to 0 eV.

Notably, the nature of the valence and conduction bands of the spinels do not change from PBE to a higher level of theory such as HSE06. For example, the valence band is always dominated by anion states (i.e., Se or S), whereas Sc^{3+} (or In^{3+} in $MgIn_2S_4$) states populate the conduction band. From Figure S3, the direct $\Gamma \rightarrow \Gamma$ band gaps obtained with PBE are $\sim$ 1.77 eV, $\sim$ 1.56 eV, and $\sim$ 1.09 eV for the $MgIn_2S_4$, $MgSc_2S_4$ and $MgSc_2Se_4$, respectively. Unsurprisingly, the magnitude of the band gaps increase when calculated with HSE06,[6] $\sim$ 2.82 eV in $MgIn_2S_4$, $\sim$ 2.63 eV in $MgSc_2S_4$, and $\sim$ 2.03 eV in $MgSc_2Se_4$, but the qualitative trends remain similar to that of PBE.

S4 0 K Phase Diagrams of Mg–A–Z

Figure S4 displays the ternary phase diagrams of (a) Mg–In–S and (b) Mg–Sc–S.

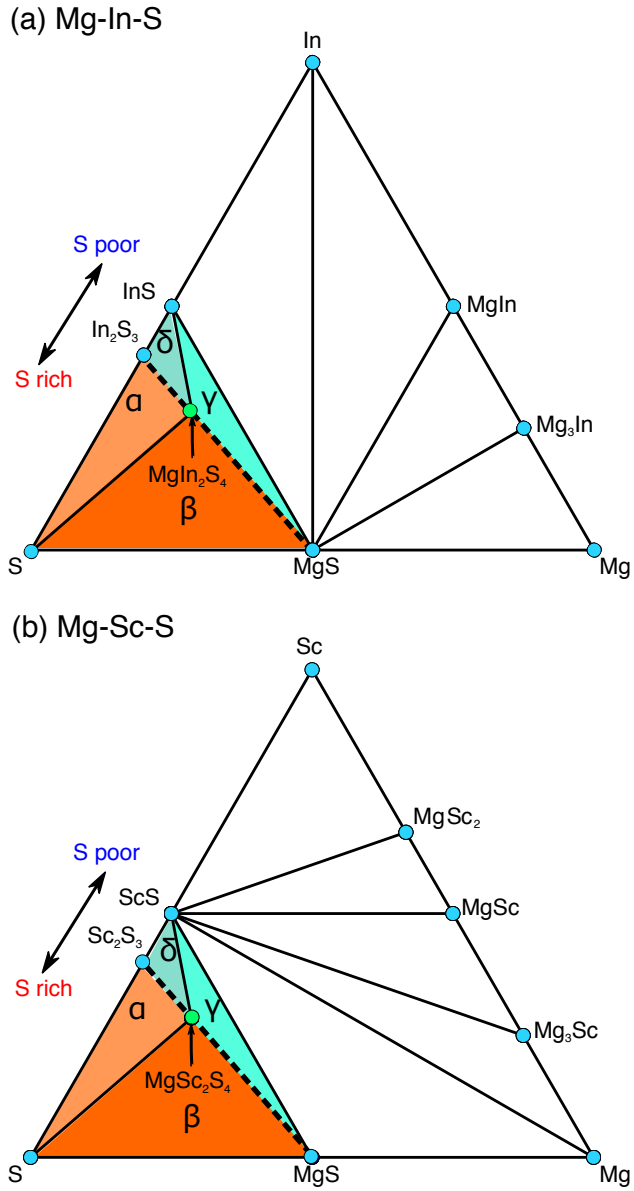

Figure S4: Ternary Mg–In–S (a) and Mg–Sc–S (b) phase-diagrams at 0 K computed from DFT data, combined with available entries from Materials Project.[7]

S5 Formation Energies of Native Defects in $MgIn_2S_4$ and $MgSc_2S_4$

Figures S5 and S6 evaluate the occurrence of intrinsic defects in $MgIn_2S_4$ and $MgSc_2S_4$ obtained across the four facets in the Mg-In-Se and Mg-Sc-S systems.

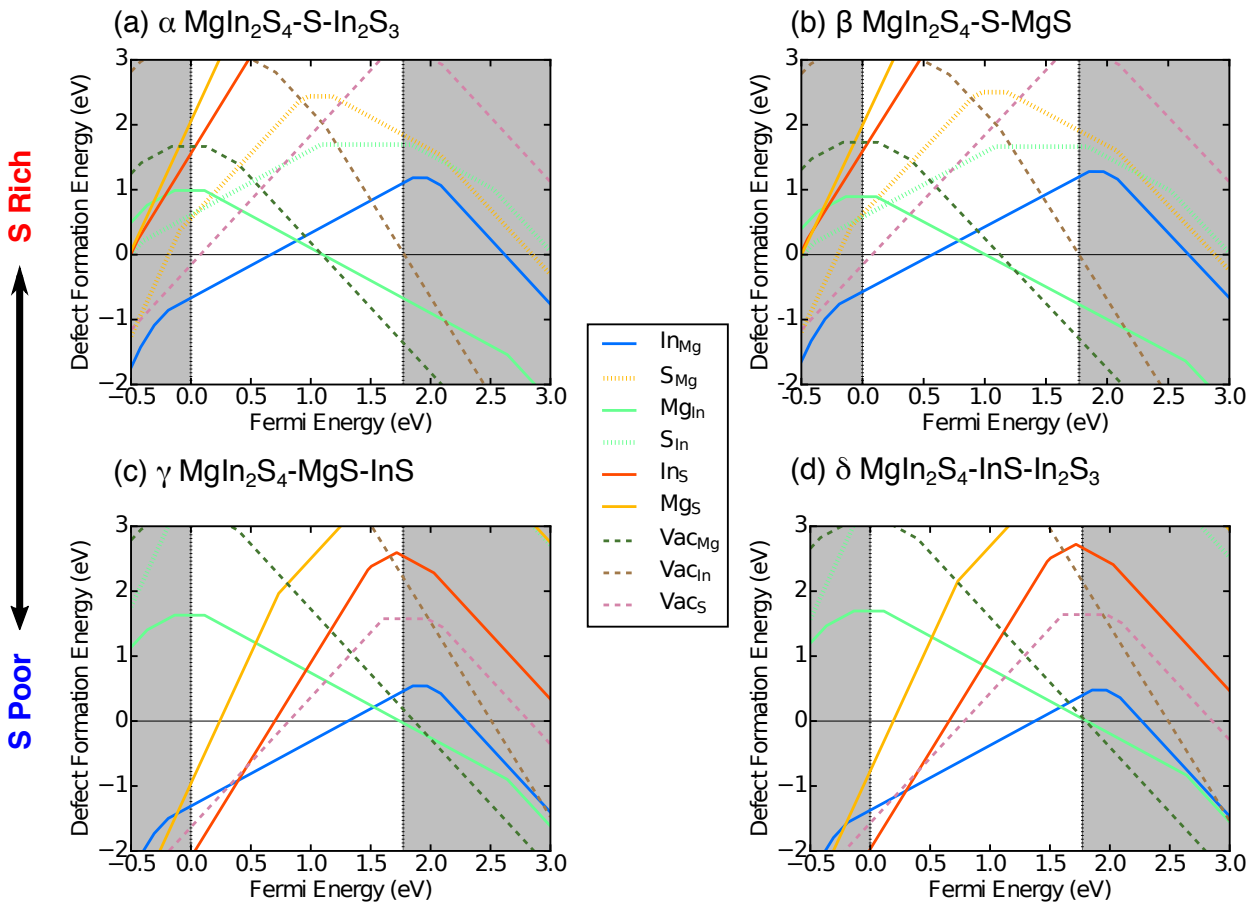

Figure S5: Defect energy $E_f[X^q]$ for intrinsic point defects (in Kröger–Vink notation) of $MgIn_2S_4$ in four facets, α, β, γ and δ (Figure S4b), of the Mg-In-S phase diagram. Regions α and β are S-rich, whereas γ and δ S-poor. The VBM is arbitrarily set to 0 eV and the white region spans the band-gap ($\sim$ 1.77 eV). Vac in the legend and dashed lines indicate vacancy defects while solid lines correspond to antisite defects.

For example, the relevant facets setting the the μ_i in Equation 1 of the manuscript are $MgIn_2S_4$-S-In_2S_3 α (Figure S5a), $MgIn_2S_4$-S-MgS β (Figure S5b), $MgIn_2S_4$-MgS-InS γ (Figure S5c), and $MgIn_2S_4$-InS-In_2S_3 δ (Figure S5d). The y-axis of each panel in Figure S5 plots the defect energy against the E_{Fermi} (x-axis) in $MgIn_2S_4$. The absolute value of the

Fermi energy is referenced to the VBM energy of the pristine $MgIn_2S_4$ bulk. The zero of the x-axis is the VBM, with grey shaded regions being the valence ($E_{Fermi} < 0$) and the conduction bands ($E_{Fermi} > E_{gap} \sim 1.77$ eV), respectively. The band gap spans the white area in all panels of Figure S5.

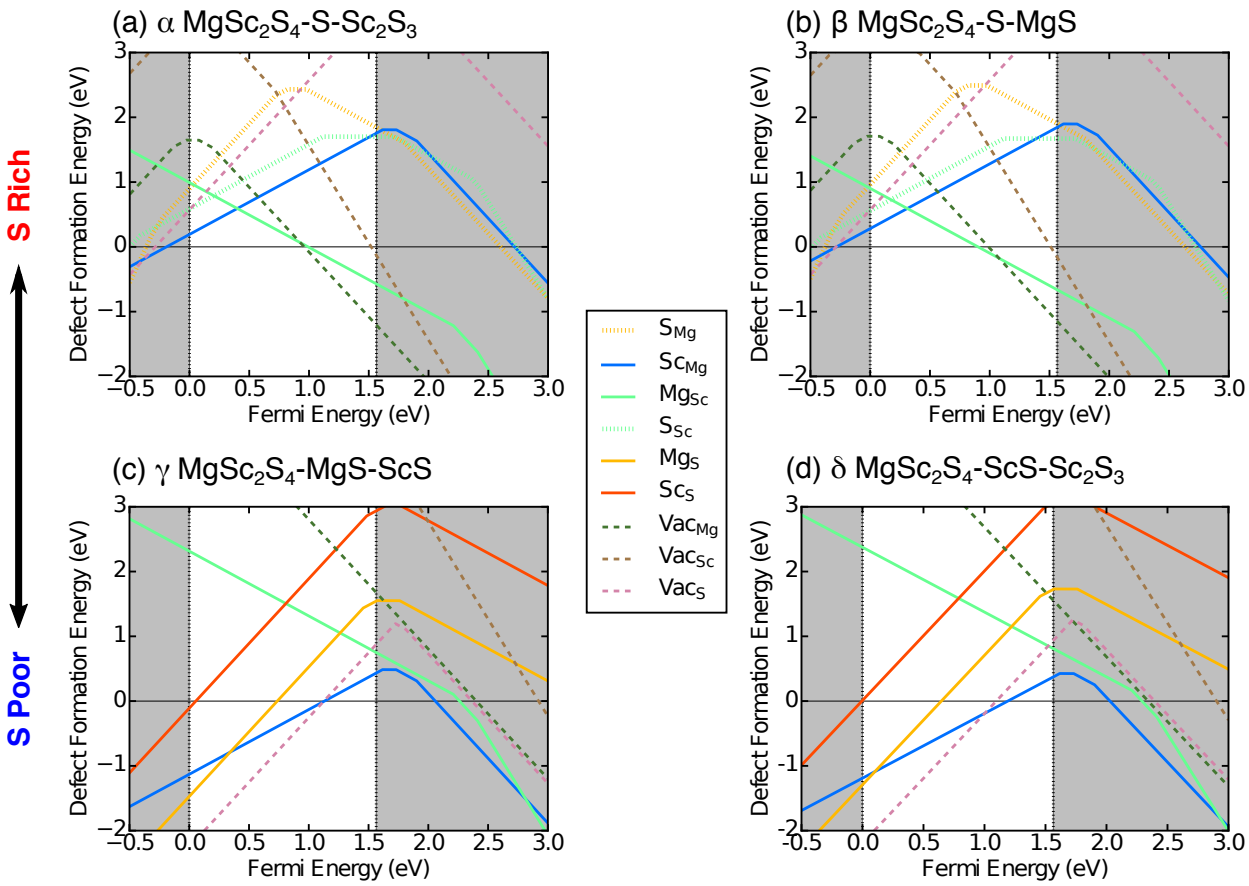

Figure S6: Defect energy $E_f[X^q]$ for intrinsic point defects (in Kröger–Vink notation) of $MgSc_2S_4$ in four facets, α, β, γ and δ (Figure S4b), of the Mg-Sc-S phase diagram. Regions α and β are S-rich, whereas γ and δ S-poor. The VBM is arbitrarily set to 0 eV and the white region spans the band-gap (~ 1.56 eV). Vac in the legend and dashed lines indicate vacancy defects while solid lines correspond to antisite defects.

S6 Equilibrium Fermi Energies and defect concentrations

Figure S7 plots the Frozen Fermi levels (E_{Fermi}^{frozen}) in $MgSc_2Se_4$ (a), $MgIn_2S_4$ (b) and $MgSc_2S_4$ (c) vs. quench temperature, for each facet of the respective ternary phase diagram. Table S1 lists the equilibrium (E_{Fermi}^{eq}) and frozen Fermi levels (for defects frozen-in from 1300 K) for each spinel and the dominant defect concentration (per cm^{-3}) for each ternary facet. Note that E_{Fermi}^{frozen} should be the same as E_{Fermi}^{eq} at a quench temperature of 300 K.

The large negative dominant defect formation energies in the S-rich facets of $MgIn_2S_4$ (Figure S7b) cause numerical difficulties in calculating the E_{Fermi}^{frozen} accurately, which explains the large fluctuations in E_{Fermi}^{frozen} with quench temperature.

Table S1: Intrinsic Fermi levels (in eV) and dominant defect concentrations (in cm^{-3}), for both the equilibrium and quenched defect scenarios are listed for all spinels and facets. The E_{Fermi}^{frozen} and $c[X^q]^{frozen}$ indicate values at 1300 K (quench temperature).

Facet	E_{Fermi}^{eq}	$c[X^q]^{eq}$	E_{Fermi}^{frozen}	$c[X^q]^{frozen}$
		$MgSc_2Se_4$		
Sc_2Se_3-Se	0.46	Sc_{Mg}: 7.99×10^{11} Mg_{Sc}: 2.35×10^{11} Vac_{Mg}: 2.82×10^{11}	–0.10	Sc_{Mg}: 2.06×10^{19} Mg_{Sc}: 1.95×10^{19} Vac_{Mg}: 2.08×10^{18}
MgSe-Se	0.27	Sc_{Mg}: 1.47×10^{11} Mg_{Sc}: 1.27×10^{12} Vac_{Mg}: 4.20×10^{2}	–0.15	Sc_{Mg}: 1.29×10^{19} Mg_{Sc}: 3.11×10^{19} Vac_{Mg}: 2.22×10^{16}
MgSe-ScSe	1.08	Sc_{Mg}: 7.96×10^{15}	1.39	Sc_{Mg}: 5.68×10^{19}
Sc_2Se_3-ScSe	1.15	Sc_{Mg}: 1.62×10^{17}	1.41	Sc_{Mg}: 1.63×10^{20}
		$MgIn_2S_4$		
In_2S_3-S	0.88	In_{Mg}: 4.90×10^{17} Mg_{In}: 4.90×10^{17} Vac_{Mg}: 7.79×10^{13}	0.10	In_{Mg}: 3.31×10^{20} Mg_{In}: 2.98×10^{20} Vac_{Mg}: 1.69×10^{19}
MgS-S	0.79	In_{Mg}: 4.90×10^{17} Mg_{In}: 4.90×10^{17} Vac_{Mg}: 3.99×10^{9}	0.07	In_{Mg}: 3.15×10^{20} Mg_{In}: 3.14×10^{20} Vac_{Mg}: 1.91×10^{18}
InS-MgS	1.53	In_{Mg}: 4.90×10^{17} Mg_{In}: 4.90×10^{17} Vac_{Mg}: 3.99×10^{9}	1.80	In_{Mg}: 3.22×10^{20} Mg_{In}: 3.07×10^{20} Vac_{Mg}: 1.83×10^{18}
In_2S_3-InS	1.59	In_{Mg}: 4.92×10^{17} Mg_{In}: 4.88×10^{17} Vac_{Mg}: 7.71×10^{13}	1.82	In_{Mg}: 3.41×10^{20} Mg_{In}: 2.90×10^{20} Vac_{Mg}: 1.60×10^{19}
		$MgSc_2S_4$		
Sc_2S_3-S	0.40	Sc_{Mg}: 1.73×10^{11} Mg_{Sc}: 3.74×10^{11} Vac_{Mg}: 2.78×10^{2}	–0.06	Sc_{Mg}: 7.07×10^{18} Mg_{Sc}: 1.91×10^{19} Vac_{Mg}: 1.01×10^{17}
MgS-S	0.35	Sc_{Mg}: 4.08×10^{10} Mg_{Sc}: 1.58×10^{12} Vac_{Mg}: 4.66×10^{-1}	–0.07	Sc_{Mg}: 5.25×10^{18} Mg_{Sc}: 2.58×10^{19} Vac_{Mg}: 2.16×10^{16}
MgS-ScS	1.48	Sc_{Mg}: 1.81×10^{15} Mg_{Sc}: 3.58×10^{7} Vac_{S}: 6.05×10^{9}	1.80	Sc_{Mg}: 6.42×10^{19} Mg_{Sc}: 2.11×10^{18} Vac_{S}: 9.45×10^{18}
Sc_2S_3-ScS	1.51	Sc_{Mg}: 5.76×10^{15} Mg_{Sc}: 1.12×10^{7} Vac_{S}: 5.86×10^{7}	1.81	Sc_{Mg}: 9.22×10^{19} Mg_{Sc}: 1.47×10^{18} Vac_{S}: 3.92×10^{18}

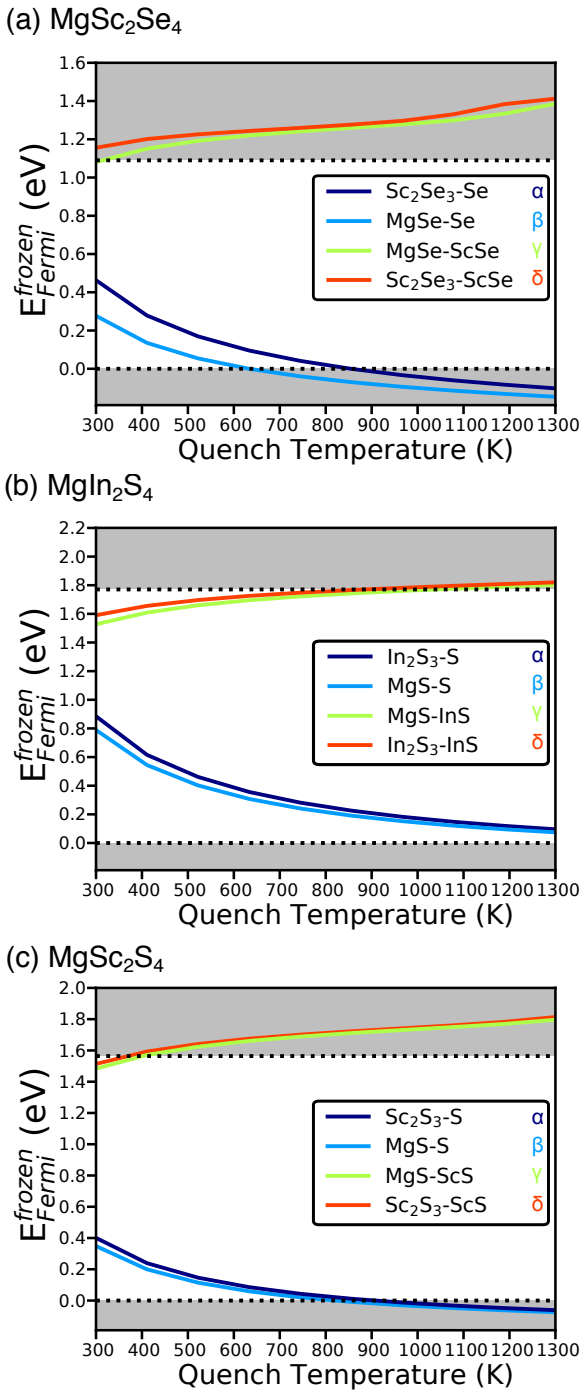

Figure S7: Fermi levels (E_{Fermi}^{frozen} in eV) at 300 K calculated for various spinels as a function of the quench temperature (in K), which correspond to the temperature at which the defect concentrations are frozen. The E_{Fermi}^{frozen} calculated at a quench temperature of 300 K is equal to the self-consistently calculated equilibrium Fermi level (E_{Fermi}^{eq}).

S7 Formation Energies of Extrinsic Defects in $MgSc_2Se_4$

Figures S8 and S9 shows the energies required to extrinsically dope several cations and anions in $MgSc_2Se_4$, across the four facets of interest ($\alpha - \delta$) in the Mg-Sc-Se system.

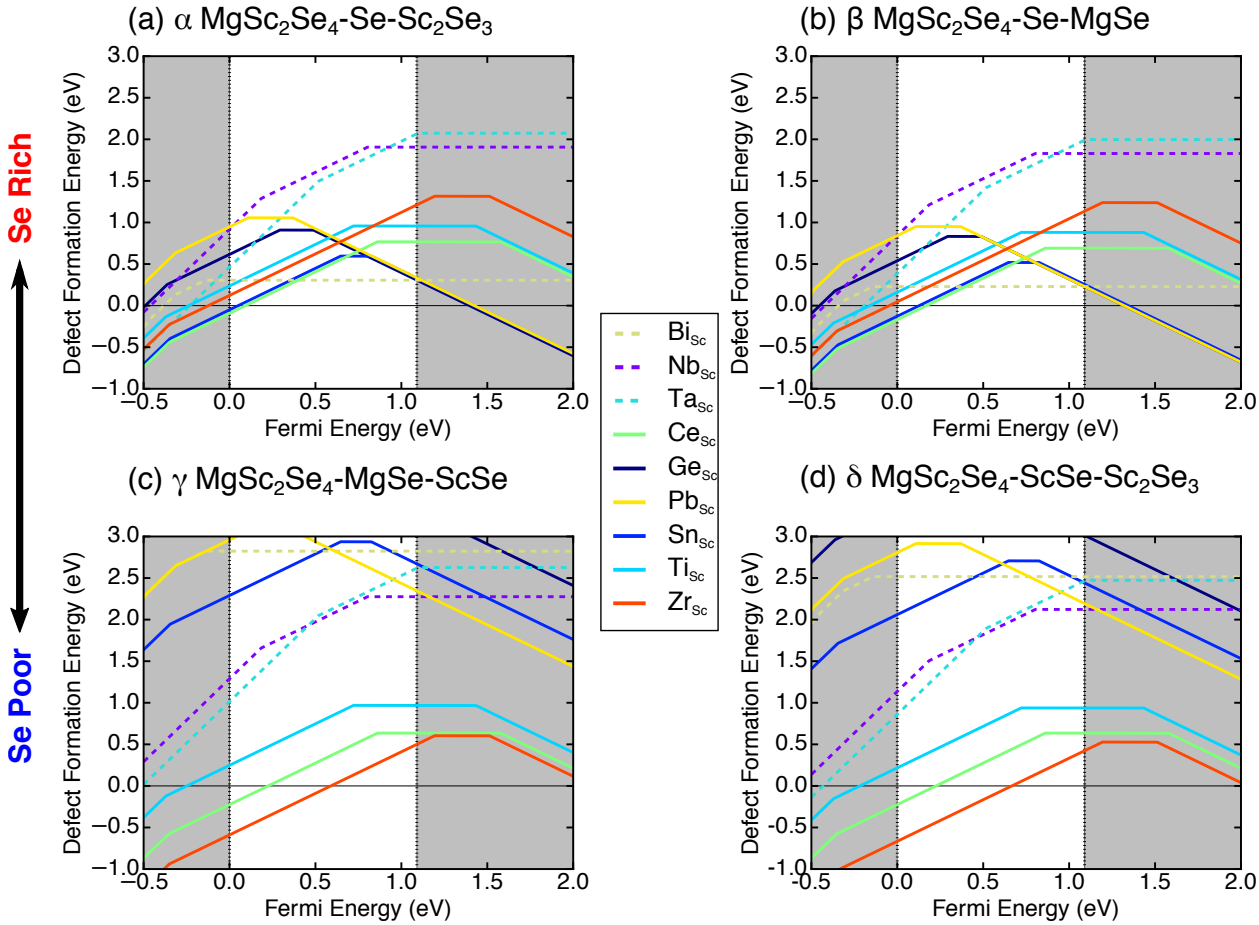

Figure S8: Formation energy $E_f[X^q]$ of extrinsic cation defects (in Kröger–Vink notation) in $MgSc_2Se_4$ in four facets, α, β, γ and δ (Figure S4a), of the Mg-Sc-Se phase diagram. Regions α and β are Se-rich, whereas γ and δ Se-poor. Tetravalent cations are shown by solid lines and pentavalent by dashed lines.

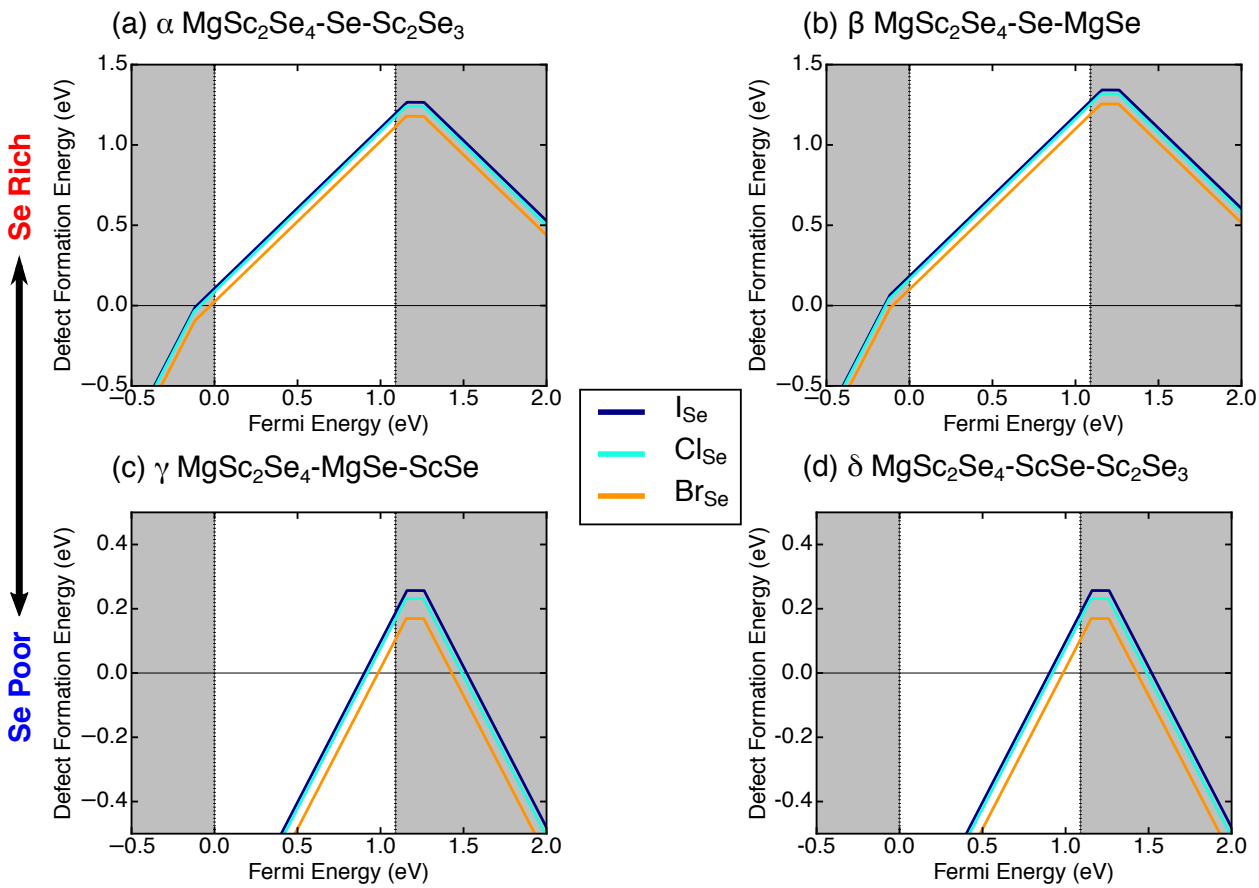

Figure S9: Formation energy $E_f[X^q]$ of extrinsic anion defects (in Kröger–Vink notation) in $MgSc_2Se_4$ in four facets, α, β, γ and δ (Figure S4a), of the Mg-Sc-Se phase diagram. Regions α and β are Se-rich, whereas γ and δ Se-poor.

S8 Dielectric tensors

Table S2 reports the diagonal component (ε_{ii}) of the computed dielectric tensor for the three cubic chalcogenide spinels.

Table S2: Diagonal components of the dielectric tensor, ε_{ii}, of $MgIn_2S_4$, $MgSc_2Se_4$ and $MgSc_2Se_4$.

component	$MgIn_2S_4$	$MgSc_2Se_4$	$MgSc_2Se_4$
$\varepsilon_{xx} = \varepsilon_{yy} = \varepsilon_{zz}$	5.02	9.17	8.24

The computed dielectric tensor for $MgIn_2S_4$ ($\sim$ 5.02) is in good agreement with the value reported experimentally ($\sim$ 5.5) by Wakaki *et al.*[8]

S9 Comparison of GGA and HSE06 defect energetics in $MgIn_2S_4$

Figures S10 shows the formation energy of the low lying intrinsic defects in $MgIn_2S_4$, across facets of interest (α and γ) in the Mg-In-S system.

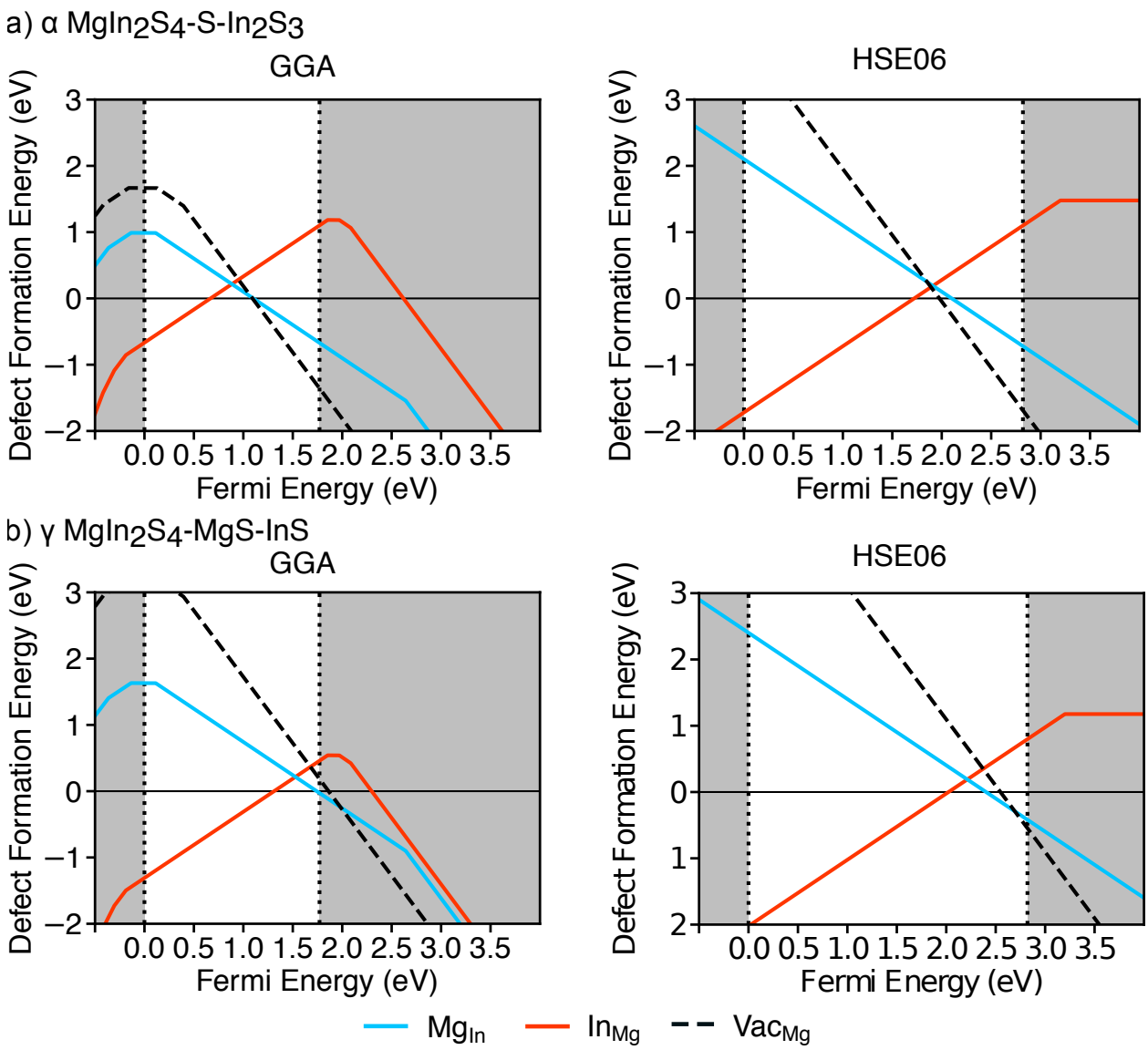

Figure S10: Comparison of formation energies $E_f[X^q]$ of low lying intrinsic defects (in Kröger–Vink notation) in $MgIn_2S_4$ in four facets, α and γ (Figure S4a), obtained with GGA and HSE06 functionals respectively. Region α is S-rich, whereas γ is S-poor.

From a qualitative comparison between GGA and HSE06, the computed concentrations of

antisite Mg_{In} and In_{Mg} defects are found similar (Figure S10a and b, Table S3) in both S-rich (α-facet) and S-poor (γ-facet) conditions. Also, the equilibrium and frozen Fermi levels ($E_{Fermi}^{eq/frozen}$) fall at similar relative fractions of the band-gap under S-poor conditions in both GGA and HSE06, while GGA and HSE06 contrastingly predict p- and n-type behavior under S-rich conditions, respectively. Nevertheless, we can confirm that GGA provides qualitatively similar conclusions to HSE06, especially with respect to the dominant defects that contribute to the electronic conductivity and spinel inversion observed in the chalcogenide Mg-conductors considered in this work.

Table S3: Comparison between the GGA and HSE06 defect energetics in the $MgIn_2S_4$ spinel, for both anion-rich (α) and anion-poor (γ) conditions (facets). Self-consistent E_{Fermi}^{eq} at 300 K (in eV) and Fermi levels with quenched defect content (from 1273 K, E_{Fermi}^{frozen}), are indicated. $c[e/h]^{eq}$ and $c[e/h]^{frozen}$ (in cm^{-3} at 300 K) are the free charge-carrier concentration in the self-consistent equilibrium and frozen defect scenarios, with e and h indicating electrons and holes. The charge of the dominant defect is indicated with respect to the charged state of the defect at E_{Fermi}^{eq}. The defect concentrations (in cm^{-3}) of the dominant defects are also shown.

Condition	Functional	Carrier	E_{Fermi}^{eq}	$c[e/h]^{eq}$	E_{Fermi}^{frozen}	$c[e/h]^{frozen}$
S-rich (α)	GGA	h^+	0.88	6.46×10^{4}	0.10	1.17×10^{18}
	HSE06	e^-	1.88	1.26×10^{2}	2.76	7.84×10^{16}
		Defect	$c[X^q]^{eq}$		$c[X^q]^{frozen}$	
	GGA	In_{Mg}	4.90×10^{17}		3.31×10^{20}	
	HSE06		2.94×10^{18}		5.62×10^{20}	
	GGA	Mg_{In}	4.90×10^{17}		2.98×10^{20}	
	HSE06		6.84×10^{17}		3.00×10^{20}	
	GGA	Vac_{Mg}	7.79×10^{13}		1.69×10^{19}	
	HSE06		1.13×10^{18}		1.31×10^{20}	
Condition	Functional	Carrier	E_{Fermi}^{eq}	$c[e/h]^{eq}$	E_{Fermi}^{frozen}	$c[e/h]^{frozen}$
S-poor (γ)	GGA	e^-	1.53	4.10×10^{14}	1.80	1.12×10^{19}
	HSE06	e^-	2.20	3.06×10^{7}	2.84	1.58×10^{18}
		Defect	$c[X^q]^{eq}$		$c[X^q]^{frozen}$	
	GGA	In_{Mg}	4.90×10^{17}		3.22×10^{20}	
	HSE06		1.42×10^{18}		4.13×10^{20}	
	GGA	Mg_{In}	4.90×10^{17}		3.07×10^{20}	
	HSE06		1.42×10^{18}		4.08×10^{20}	
	GGA	Vac_{Mg}	3.99×10^{9}		1.83×10^{18}	
	HSE06		4.12×10^{9}		1.95×10^{18}	

References

(1) Freysoldt, C.; Neugebauer, J.; de Walle, C. G. V. *Physica Status Solidi B* **2010**, *248*, 1067–1076.

(2) Freysoldt, C.; Grabowski, B.; Hickel, T.; Neugebauer, J.; Kresse, G.; Janotti, A.; de Walle, C. G. V. *Rev Mod Phys* **2014**, *86*, 253–305.

(3) Perdew, J. P.; Burke, K.; Ernzerhof, M. *Phys Rev Lett* **1996**, *77*, 3865–3868.

(4) Heyd, J.; Scuseria, G. E.; Ernzerhof, M. *The Journal of Chemical Physics* **2003**, *118*, 8207–8215.

(5) Heyd, J.; Scuseria, G. E.; Ernzerhof, M. *The Journal of Chemical Physics* **2006**, *124*, 219906.

(6) Chevrier, V. L.; Ong, S. P.; Armiento, R.; Chan, M. K. Y.; Ceder, G. *Phys Rev B* **2010**, *82*.

(7) Jain, A.; Ong, S. P.; Hautier, G.; Chen, W.; Richards, W. D.; Dacek, S.; Cholia, S.; Gunter, D.; Skinner, D.; Ceder, G. et al. *APL Materials* **2013**, *1*, 011002.

(8) Wakaki, M.; Shintani, O.; Ogawa, T.; Arai, T. *Japanese Journal of Applied Physics* **1980**, *19*, 255.